Imaging a crustal low-velocity layer using reflected seismic waves from the 2014 earthquake swarm at Long Valley Caldera, California: the magmatic system roof?

Nori Nakata[1] and David R. Shelly[2]

Keypoints

- Clear reflections are observed during 2014 Long Valley Caldera earthquake swarm.
- We apply wavefield migration to the reflections to image the reflector using a single station.
- The reflector is likely related to the top of the contemporary magmatic system at 8.2 km depth.

[1]University of Oklahoma, Norman, Oklahoma, USA

[2]U.S. Geological Survey, Menlo Park, California, USA

The waveforms generated by the 2014 Long Valley Caldera earthquake swarm recorded at station MLH show clear reflected waves that are often stronger than direct P and S waves. With waveform analyses, we discover that these waves are reflected at the top of a low velocity body, which may be residual magma from the ∼767 ka caldera-forming eruption. The polarity of the reflection compared to direct P and S waves suggests that the reflection is SP waves (S from hypocenters to reflector and then convert to P waves to the surface). Because the wavefields are coherent among different earthquakes and hold high signal-to-noise ratios, we apply them to a wavefield migration method for imaging reflectors. The depth of the imaged magmatic-system roof is around 8.2 km below the surface. This is consistent with previous studies. Even though we use only one station and waveforms from one earthquake swarm, the dense cluster of accurately located earthquakes provides a high-resolution image of the roof.

1. Introduction

Long Valley Caldera in California has been studied intensively for decades [*Hill et al.*, 2017]. *Bailey et al.* [1976] and *Hill* [1976] discussed the geological and geophysical structure of Long Valley Caldera and its eruption history. A persistent focus of research has been the location and activity of magma [*Ryall and Ryall*, 1981; *McConnel et al.*, 1995; *Hildreth*, 2004; *Peacock et al.*, 2016]. A combination of volcanic and tectonic forces generates high rates of seismicity, including frequent earthquake swarms. *Savage and Clark* [1982] studied the 1980 **M**6 earthquakes and concluded that the earthquakes were triggered by magmatic resurgence. Fine fault structure, stress regions, and interaction of volcanic fluid have been revealed by the precise analyses of these swarms especially in 1997 and 2014 [*Prejean et al.*, 2002; *Shelly et al.*, 2015]. The swarms at Long Valley contain brittle $\sim$ long-period earthquakes at a variety of depths [*Hill et al.*, 2002; *Shelly and Hill*, 2011].

The 2014 Long Valley earthquake swarm was the most active swarm in the caldera since 1997, with more than 3300 routinely cataloged events from June–October, 2014. In this study, we use a portion of the earthquake swarm (811 events) that mostly occurred on July 7–8 and September 26, detected and located by *Shelly et al.* [2016a] (Figure 1). The events used here are detected by using one template earthquake (**M**1.51 event at 2:35AM UTC, 10 July 2014) and most of the events used have very similar left-lateral strike-slip focal mechanisms [*Shelly et al.*, 2016b]. The earthquakes detected by this template show higher signal-to-noise ratio (SNR) of our target waves. We focus on the wavefields of these events observed at station MLH (which has only vertical component) in the Northern California

Seismic Network (the green triangle in Figure 1). A wave that has distinct moveout from direct waves is clearly observed when events are sorted by source depth (the red arrow in Figure 2b), and as we discuss later, this is likely a reflected wave from the upper surface of a low-velocity body, which could be a zone of partial melt and/or accumulated magmatic fluids. Note that although reflected waves with active sources and/or other earthquakes at Long Valley Caldera have been studied [*Hill*, 1976; *Hill et al.*, 1985; *Luetgert and Mooney*, 1985; *Stroujkova and Malin*, 2000], the waveforms in Figure 2b are exceptionally vivid. Here, we examine the features of the wave and use it for imaging.

For imaging, we apply a wavefield migration technique (reverse time migration; RTM), which is often used for active-source imaging, to the earthquake swarm seismograms recorded at station MLH. The idea of using earthquake waveforms for imaging reflectors with migration has been implemented previously [e.g., *Stroujkova and Malin*, 2000; *Reshetnikov et al.*, 2010; *Hrubcová et al.*, 2016]. Compared to the reflected waves on the west-side of Long Valley Caldera used by *Stroujkova and Malin* [2000], our earthquake sources are dense and waveforms show coherent reflections. We use the source information (locations and mechanisms) given by *Shelly et al.* [2016a, b], who estimated precise locations and mechanisms of each event with wavefield correlation.

In this study, we start with the discussion of the detail of the observed wavefields using time shift, 3D beamforming and waveform averaging. Then we apply RTM to the wavefields and discuss the imaged reflector.

2. Observation of reflected waves

2.1. Observed waves

We first examine the observed waveforms at station MLH (Figure 2). In addition to the P, S, and their reverberating coda, this station recorded prominent reflected waves. When we align the recorded waveforms with the estimated event origin time (Figure 2a), the reflected wave exists at 2.5–3 s, although other phases contaminate to make the visual identification harder. The reflected waves are coherent and well recognized in the waveforms aligned on S-wave phases around 3–6 s (Figure 2b). The alignment is based on the time lags of maximum crosscorrelation values between the template earthquake and others within this time window. The direct-arrival phases show nearly linear moveout, and the reflected phase has non-linear moveouts. The reflected wave is mostly observed between the direct P and S waves except for shallower events, where the reflected waves arrive after S waves. The arrival times of waves suggest that the reflector is located below the source region, and the reflected waves are first propagated downward from the hypocenters, then scattered upward toward the surface. A coherent wave at around 2.6 s from shallower events is likely an S-to-P converted wave at near surface (probably at the layer of the volcanic tuff at around 2 km depth) based on the V_p/V_s ratio (black arrow on Figure 2b).

The ray path of the reflected waves is also confirmed from the source-side 3D beamforming (Appendix A). Based on the depth slownesses of direct and reflected waves, the reflected waves first propagate downward, reflect at a reflector, and then propagate towards the ground surface (Figure S1). The strong reflector beneath the source region at 6–7 km depth might be related to the partial-melt volume of the residual Bishop magma remaining after the caldera-forming eruption ∼767 ka [*Crowley et al.*, 2007], which would be a low-velocity volume [*Dawson et al.*, 1990; *Weiland et al.*, 1995; *Seccia et al.*, 2011]. *Black et al.* [1991] argued that the reflections studied by *Hill* [1976] are likely caused by the caldera wall. We can exclude this possibility based on the radiation angle of the reflected wave from the beamforming result (Figure S1).

2.2. Amplitude and polarity

Observed S-wave amplitudes are stronger than P waves even though we use the vertical component (Figure 2). Based on focal mechanisms determined by *Shelly et al.* [2016b], the direct P waves recorded at station MLH radiate from near the nodal plane. When S-wave radiation angle is similar, the S wave can be stronger even when recorded on the vertical component (Appendix B). Interestingly, the reflected waves have the highest amplitude among the three waves highlighted in Figure 2; despite the fact that reflected waves lose more energy than the direct waves during wave propagation because of incomplete reflection and a longer wave path.

To understand the strong amplitude of the reflection, we analyze the phase of this wave. Because the reflected wave arrives between P and S direct waves in time, this wave travels as a P wave for the majority of the path and is recorded on the vertical component (Figure S2); hence the wave is either PP or SP waves (first letter represents the wave type along the path from the source to the reflector, and the second from the reflector to the receiver). *Stroujkova and Malin* [2000] studied the reflected waves on the west side of the caldera, and they found that the frequency content of the reflected waves is lower than P waves and similar to S waves; therefore they concluded that the waves they analyzed were SP waves. In our data, however, we do not find a consistent difference in frequencies between P and reflected waves (Figure S3) as well as for P and S waves.

For the vertical component with a nearly strike-slip earthquake and the radiation angle computed by *Shelly et al.* [2016b], direct P and S waves have opposite polarity, P and PP waves also have opposite polarity, and P and SP waves have the same polarity when the velocity below the reflector is lower (the cartoons in Figure 3). Because the focal mechanisms for most of the earthquakes in this cluster are similar [*Shelly et al.*, 2016b], we assume that the polarities of observed waves do not vary much among different earthquakes. To estimate accurate polarity changes, we compute averaged P, reflected, and S wavelets over all earthquakes by using waveforms around the travel times of each wave shown in Figure S2 (Figure 3). Then we compute crosscorrelation coefficients between each wavelet; maximum coefficients as absolute value are 0.934 (P and reflection: positive), -0.772 (reflection and S: negative) and -0.836 (P and S: negative). Although polarity changes between these wavelets are not very clear, the positive and negative correlation coefficients suggest that the reflected wave is indeed an SP wave.

This suggestion of SP wave is also supported by the amplitude of the reflection (Appendix B). If the reflector is nearly horizontal, excitation energy for a PP wave is small, similar to the direct P wave (excitation point is close to the nodal plane). The SP wave is excited as an S wave, stronger than a P wave, converted to a P wave at the reflector, and observed in the vertical component of station MLH as a P wave, with a greater portion of its energy vertically polarized compared to the direct S wave. Therefore, the SP reflection can be stronger than direct P or S waves. In Appendix B, we analytically compute amplitude ratios between different waves and confirm that the SP wave would be significantly stronger than the PP wave, and the amplitude of the SP wave is in the same order of direct P and S waves.

3. Imaging reflectors with wavefield migration

We use a wavefield migration method to image the reflectors with the SP wave [*Claerbout*, 1985]. We solve the two-way wave equation and apply reverse-time migration (RTM) to include the possibility that the reflectors are above the source regions or are vertically oriented [*Hale et al.*, 1992]. RTM is a technique to image subsurface reflectors: first we numerically reconstruct wavefields from sources and receivers, respectively (these waves meet at the location of scatterers/reflectors), and then crosscorrelate these reconstructed wavefields to image reflectors [*Baysal et al.*, 1983; *Sava and Hill*, 2009; *Nakata and Beroza*, 2016]. For the reconstruction of the wavefields, we need a velocity model. In this region, several velocity models have been proposed in both 1D and 3D (e.g., 1D: *Sanders and Nixon* [1995]; *Stroujkova and Malin* [2000]; *Prejean et al.* [2002], 3D: *Hill et al.* [1985]; *Kissling* [1988]; *Fliedner et al.* [2000]; *Seccia et al.* [2011]; *Lin* [2015]). We use the 1D velocity model proposed by *Stroujkova and Malin* [2000] and add three layers from 0–1 km depth shown in *Prejean et al.* [2002] (Table S1).

With this 1D velocity model, we apply RTM in 2D (slice of each degree of azimuth) but not 3D because horizontal slownesses are preserved. For the 2D RTM at each degree of azimuth, we first choose earthquakes that occur in this degree range (e.g., 224.5°–225.5°). After the 2D RTM for all azimuths, we concatenate 2D slices to generate a 3D image of the subsurface. To reconstruct wavefields, we use reciprocity of the data; we numerically back-propagate observed waveforms from each hypocenter simultaneously with S-wave velocities and forward-propagate a Ricker wavelet (peak frequency of 10 Hz) from the receiver location with P-wave velocities (see the cartoon in Figure 4). This simulates the SP propagation. For each wave, we solve the pseudo acoustic wave equation with finite difference by ignoring wave conversions from source/receiver to the reflector. Then we compute crosscorrelation of these wavefields to construct a reflection image (Figure 4a–c). Here we take the Born approximation and ignore higher-order scattered waves. As similar to Figure S1, we use synthetic data as a reference (Figure 4a). When we use the entire observed wavefields for RTM (Figure 4c), the image contains lots of signals which contaminate our interpretation of the target reflection. Hence, we deterministically apply time windows to isolate waves around the reflected wave (± 1 s from the travel times shown in Figure S2) and focus images related to our target reflectors (Figure 4b). The limited source-receiver aperture results in an egg-shaped image, but with the help of the synthetic image (Figure 4a) and spatial continuity using different azimuths, the strong amplitudes at 3 km distance and 8.2 km depth are likely the reflector producing the strong reflected wave (the white arrow in Figure 4b).

After computing images for all available azimuths (219°–243°), we construct the 3D view of the reflectors (Figure 4d). Although it reduces the spatial resolution, we compute the 2D envelope at each azimuth and use 3D smoothing (Gaussian filter with (100m,100m,3°)) to smoothly connect each 2D image. Also, to further improve SNR, we create a binary mask that has a value of 1.0 where the envelope intensity of synthetic images after smoothing is larger than 0.1 and 0 everywhere else, and then multiply the mask to the 3D image.

The result illustrated in Figure 4d shows that a strong reflector exists around 8.2±0.1 km depth, where the silver isosurface is illustrated. The depth uncertainty is based on the thickness of the high intensity area (>0.9 normalized intensity).

4. Discussion

As we inferred from beamforming (Figure S1), the reflector is located deeper than the source region (Figure 4d). We conclude that this reflector is the top of a low-velocity zone. Evidence for the low-velocity zone at similar depths has been reported in several previous studies, and is usually interpreted as a partial-melt volume of the Bishop magma or accumulated magmatic fluids [*Hill*, 1976; *Stroujkova and Malin*, 2000; *Seccia et al.*, 2011]. The roof of this magmatic system would be expected to present an unusually large velocity anomaly in the crust. Because of the location of the earthquake swarm and the receiver used, we cannot determine the horizontal extent of the reflector much beyond MLH (Figure 4). However, the continuity of images into the azimuth direction indicates that our technique works well to coherently image the reflector because the earthquakes used in each azimuth are independent. Kinematically this image constrains the upper surface of the low-velocity structure with higher resolution (depth of 8.1–8.3 km). By contrast, local-earthquake tomographic imaging of such structure would be challenging because waves generated by shallow local earthquakes do not directly sample these structures. In principle, we could compute the reflection coefficients of the reflector from the image, but we would have to account for attenuation (both scattering and intrinsic) of seismic waves with better knowledge of the attenuation structure.

Although our preferred interpretation is that of SP reflection, we consider the possibility that the reflections in Figure 2 are PP reflections. Under this assumption, the depth of the reflector becomes about 1.0 km deeper than Figure 4, because the P velocities are higher than S velocities (Figure S4). The quality of the image is about equal to the SP case (reflection points are well focused). However, based on the information of amplitudes (Figure 2, Appendix B), polarity (Figure 3), and source mechanisms of events [*Shelly et al.*, 2016b], we conclude that the interpretation of SP waves is most reasonable and prefer the image shown in Figure 4.

Interestingly, the reflected waves at station MLH are much more prominent than at stations MDR or MLAC, which are closer to the swarm. *Seccia et al.* [2011] found evidence for a low-velocity layer below station MLAC, suggesting that the reflector may extend there. We speculate that the weakness of these waves at stations MDR or MLAC is due to the radiation pattern of the swarm earthquakes. The small offset requires vertically propagating waves to produce strong reflections, but for strike-slip events, such waves are weak. More distant stations would presumably capture the waves reflected from the bottom of the low-velocity volume as in *Luetgert and Mooney* [1985].

The methods used here could be applied to other areas in and out the Long Valley Caldera to characterize reflected waves and map reflectors. Dense earthquake swarms are helpful to identify reflections. The knowledge of the accurate location of earthquakes is important, and focal mechanisms are used for the interpretation of wave types but not needed for imaging. We require sufficiently high SNR of reflected waves for imaging, and hence we need stations at right spots especially for strike-slip earthquakes such as close enough to have high SNR but not to close to the nodal plane.

5. Conclusion

We analyze prominent non-direct waves observed during the 2014 Long Valley Caldera earthquake swarm. These waves clearly have a different moveout than the direct P or S waves. Beamforming of wavefields suggests that the waves are reflected at a boundary located beneath the swarm-source volume, which is likely related to the top of the residual Bishop magmatic system. Based on the amplitude of the waves and their polarity, we conclude that the waves are SP reflections. We apply a wavefield-migration technique to the reflected waves to find the location of reflectors. The roof is imaged at 8.2 km depth, which is roughly corresponding to previous studies. We use synthetic waveforms (travel times of reflected waves) as a reference to interpret the beamforming and imaging results to overcome the limited aperture of source-receiver locations and SNR, and hence we can extract the information of magmatic system using waves from densely clustered earthquakes recorded on a single receiver.

Acknowledgments. We thank people who operate seismic stations at the Long Valley region especially for station MLH operated by the USGS and make the data available through the Northern California Earthquake Data Center (NCEDC), doi:10.7932/NCEDC. We also thank Walter D. Mooney, Ashton Flinders, and David Hill for their fruitful comments. We appreciate two anonymous reviewers and the GRL editor Jeroen Ritsema to improve the quality of this study. We are grateful to the Madagascar

project to freely provide the software for applying RTM [*Fomel et al.*, 2013]. To process the data, we use the Oscer cluster at the University of Oklahoma.

References

Bailey, R. A., G. B. Dalrymple, and M. A. Lanphere, Volcanism, structure, and geochronology of Long Valley Caldera, Mono County, California, *J. Geophys. Res.*, *81*(5), 725–744, 1976.

Baysal, E., D. D. Kosloff, and J. W. C. Sherwood, Reverse time migration, *Geophysics*, *48*(11), 1514–1524, 1983.

Black, R. A., S. J. Deemer, and S. B. Smithson, Seismic reflection studies in Long Valley Caldera, California, *J. Geophys. Res.*, *96*(B3), 4289–4300, 1991.

Claerbout, J. F., *Imaging the Earth's interior*, Blackwell Science Inc, 1985.

Crowley, J. L., B. Schoene, and S. A. Browring, U-Pb dating of zircon in the Bishop Tuff at the millennial scale, *Geology*, *35*(12), 1, 2007.

Dawson, P. B., J. R. Evans, and H. M. Iyer, Teleseismic tomography of the compressional wave velocity structure beneath the Long Valley region, California, *J. Geophys. Res.*, *95*(B7), 11,021–11,050, 1990.

Fliedner, M. M., S. L. Klemperer, and N. I. Christensen, Three-dimensional seismic model of the Sierra Nevada arc, California, and its implications for crustal and upper mantle composition, *J. Geophys. Res.*, *105*(B5), 10,899–10,921, 2000.

Fomel, S., P. Sava, I. Vlad, Y. Liu, and V. Bashkardin, Madagascar: ope-source software project for multidimensional data analysis and reproducible computational experiments, *J. Open Res. Software*, *1*(1), e8, 2013.

Hale, D., N. R. Hill, and J. Stefani, Imaging salt with turning seismic waves, *Geophysics*, *57*(11), 1453–1462, 1992.

Hildreth, W., Volcanological perspectives on Long Valley, Mammoth Mountain, and Mono Craters: several contiguous but discrete systems, *J. Volcanol. Geoth. Res.*, *136*, 169–198, 2004.

Hill, D. P., Structure of Long Valley Caldera, California, from a seismic refraction experiment, *J. Geophys. Res.*, *81*(5), 745–753, 1976.

Hill, D. P., E. Kissling, J. H. Luetgert, and U. Kradolfer, Constraints on the upper crustal structure of the Long Valley – mono craters volcanic complex, Eastern California, from seismic refraction measurements, *J. Geophys. Res.*, *90*(B13), 11,135–11,150, 1985.

Hill, D. P., P. Dawson, M. J. S. Johnson, A. M. Pitt, G. Biasi, and K. Smith, Very-long-period volcanic earthquakes beneath Mammoth Mountain, California, *Geophys. Res. Lett.*, *29*(10), 1370, 2002.

Hill, D. P., M. T. Mangan, and S. R. McNutt, Volcanic unrest and hazard communication in Long Valley volcanic region, California, *Advances in Volcanology*, pp. 1–17, 2017.

Hrubcová, P., V. Vavryčuk, A. Boušková, and M. Bohnhoff, Shallow crustal discontinuities inferred from waveforms of microearthquakes: Method and application to KTB drill site and West Bohemia swarm area, *J. Geophys. Res.*, *121*, 881–902, doi: 10.1002/2015JB012548, 2016.

Kissling, E., Geotomography with local earthquake data, *Rev. Geophysics*, *26*(4), 659–698, 1988.

Lin, G., Seismic velocity structure and earthquake relocation for the magmatic system beneath Long Valley Caldera, eastern California, *J. Volcanol. Geotherm. Res.*, *296*, 19–30, 2015.

Luetgert, J. H., and W. D. Mooney, Crustal refraction profile of the Long Valley Caldera, California, from the January 1983 Mammoth Lakes earthquake swarm, *Bull. Seismol. Soc. Am.*, *75*(1), 211–221, 1985.

McConnel, V. S., C. K. Shearer, J. C. Eichelberger, M. J. Keskinen, P. W. Layer, and J. J. Papike, Rhyolite intrusions in the intracaldera Bishop Tuff, Long Valley Caldera, California, *J. Volcanol. Geotherm. Res.*, *67*, 41–60, 1995.

Nakata, N., and G. C. Beroza, Reverse-time migration for microseismic sources using the geometric mean as an imaging condition, *Geophysics*, *81*(2), KS51–KS60, 2016.

Peacock, J. R., M. T. Mangan, D. McPhee, and P. E. Wannamaker, Three-dimensional electrical resistivity model of the hydrothermal system in Long Valley Caldera, California, from magnetotellurics, *Geophys. Res. Lett.*, *43*, 7953–7962, 2016.

Prejean, S., W. Ellsworth, M. Zoback, and F. Waldhauser, Fault structure and kinematics of the Long Valley Caldera region, California, revealed by high-accuracy earthquake hypocenters and focal mechanism stress inversions, *J. Geophys. Res.*, *107*(B12), 2355, doi:10.1029/2001JB001168, 2002.

Reshetnikov, A., S. Buske, and S. A. Shapiro, Seismic imaging using microseismic events: Results from the San Andreas Fault System at SAFOD, *J. Geophys. Res.*, *115*, B12,324, 2010.

Ryall, F., and A. Ryall, Attenuation of P and S waves in a magma chamber in Long Valley Caldera, California, *Geophys. Res. Lett.*, *8*(6), 557–560, 1981.

Sanders, C. O., and L. D. Nixon, S wave attenuation structure in Long Valley caldera, California, from three-component S-to-P amplitude ratio data, *J. Geophys. Res.*, *100*(B7), 12,395–12,404, 1995.

Sava, P., and S. J. Hill, Overview and classification of wavefield seismic imaging methods, *The Leading Edge*, *28*, 170 – 183, 2009.

Savage, J. C., and M. M. Clark, Magmatic resurgence in Long Valley Caldera, California: Possible cause of the 1980 Mammoth Lakes Earthquakes, *Science*, *217*, 531–533, 1982.

Seccia, D., C. Chiarabba, P. D. Gori, I. Bianchi, and D. P. Hill, Evidence for the contemporary magmatic system beneath Long Valley Caldera from local earthquake tomography and receiver function analysis, *J. Geophys. Res.*, *116*, B12,314, doi: 10.1029/2011JB008471, 2011.

Shelly, D. R., and D. P. Hill, Migrating swarms of brittle-failure earthquakes in the lower crust beneath Mammoth Mountain, California, *Geophys. Res. Lett.*, *38*, L20,307, 2011.

Shelly, D. R., T. Taira, S. G. Prejean, D. P. Hill, and D. S. Dreger, Fluid-faulting interactions: Fracture-mesh and fault-valve behavior in the February 2014 Mammoth Mountain, California, earthquake swarm, *Geophys. Res. Lett.*, *42*, 5803–5812, doi: 10.1002/2015GL064325, 2015.

Shelly, D. R., W. L. Ellsworth, and D. P. Hill, Fluid-faulting evolution in high definition: Connecting fault structure and frequecy magnitude variations during the 2014 Long Valley Caldera, California, earthquake swarm, *J. Geophys. Res.*, *121*, 1776–1795, doi:

10.1002/2015JB012719, 2016a.

Shelly, D. R., J. L. Hardebeck, W. L. Ellsworth, and D. P. Hill, A new strategy for earthquake focal mechanisms using waveform-correlation-derived relative polarities and cluster analysis: Application to the 2014 Long Valley Caldera earthquake swarm, *J. Geophys. Res.*, *121*, 8622–8641, 2016b.

Stroujkova, A. F., and P. E. Malin, A magma mass beneath Casa Diablo? Further evidence from reflected seismic waves, *Bull. Seismol. Soc. Am.*, *90*(2), 500–511, 2000.

Watanabe, T., Effects of water and melt on seismic velocities and their application to characterization of seismic reflectors, *Geophys. Res. Lett.*, *20*(24), 2933–2936, 1993.

Weiland, C. M., L. K. Steck, P. B. Dawson, and V. A. Korneev, Nonlinear teleseismic tomography at Long Valley caldera, using three-dimensional minimum travel time ray tracing, *J. Geophys. Res.*, *100*(B10), 20,379–20,390, 1995.

Wyering, L. D., M. C. Villeneuve, I. C. Wallis, P. A. Siratovich, B. M. Kennedy, D. M. Gravley, and J. L. Cant, Mechanical and physical properties of hydrothermally altered rocks, Taupo Volcanic Zone, New Zealand, *J. Volcanol. Geoth. Res.*, *288*, 76–93, 2014.

List of figures

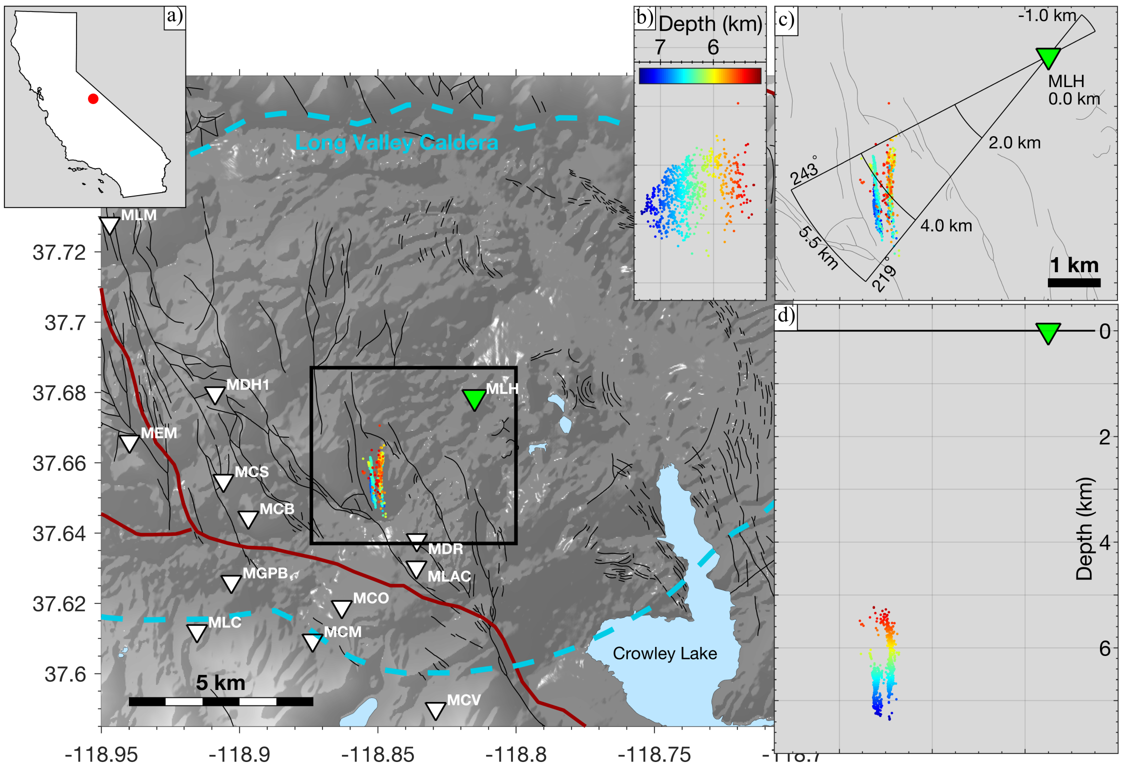

Figure 1. Map of the Long Valley Caldera with seismometers (reverse triangle) and located earthquakes used in this study (dots colored by depth). The green triangle (MLH) highlights the station we used. The dashed cyan, thin black, and dark red lines illustrate the boundary of the caldera, mapped faults, and roads respectively. (a) Map of California with the location of the Long Valley with the red dot. (b) Cross-section (latitude–depth) of hypocenters. The depth is referenced to the elevation 2.2 km above sea level (i.e., average ground surface around this area). (c) Magnified map of the area of the thick black rectangle in the main map. The black fan-shaped lines are the axes used in Figure 4. (d) Cross-section (longitude–depth) of hypocenters. The horizontal black line indicates the ground surface. Insets (b–d) share the scale and axes, and have no exaggeration.

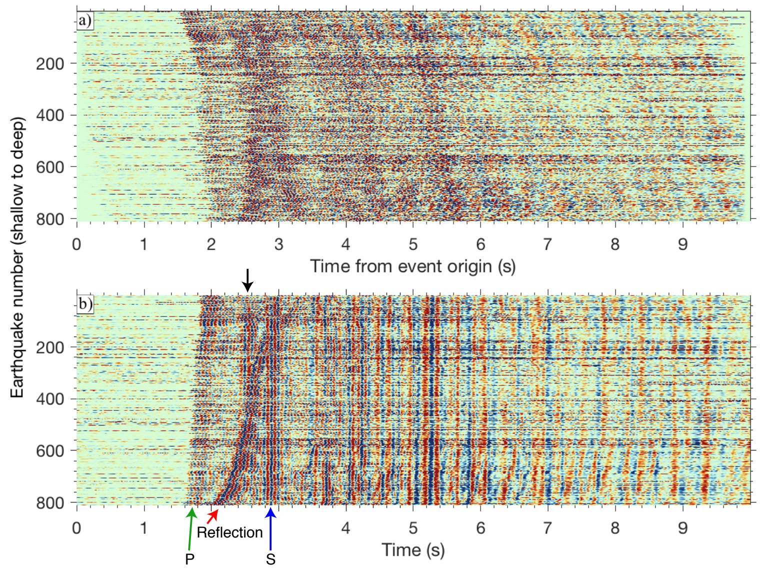

Figure 2. (a) Observed waveforms at station MLH (vertical component filtered 2–15 Hz) aligned by the estimated earthquake origin times. The event waveforms are ordered by the relocated depth with the smaller earthquake numbers indicating shallower events. Red and blue indicate positive and negative amplitudes, respectively. The amplitudes of waves are normalized at each trace. (b) Same waveforms as panel (a) after aligning based on wavelets around 3–6 s. The P, reflected, and S waves stand out clearly as indicated by the green, red and blue arrows, respectively. The black arrow highlights the S-to-P converted wave at 2 km depth.

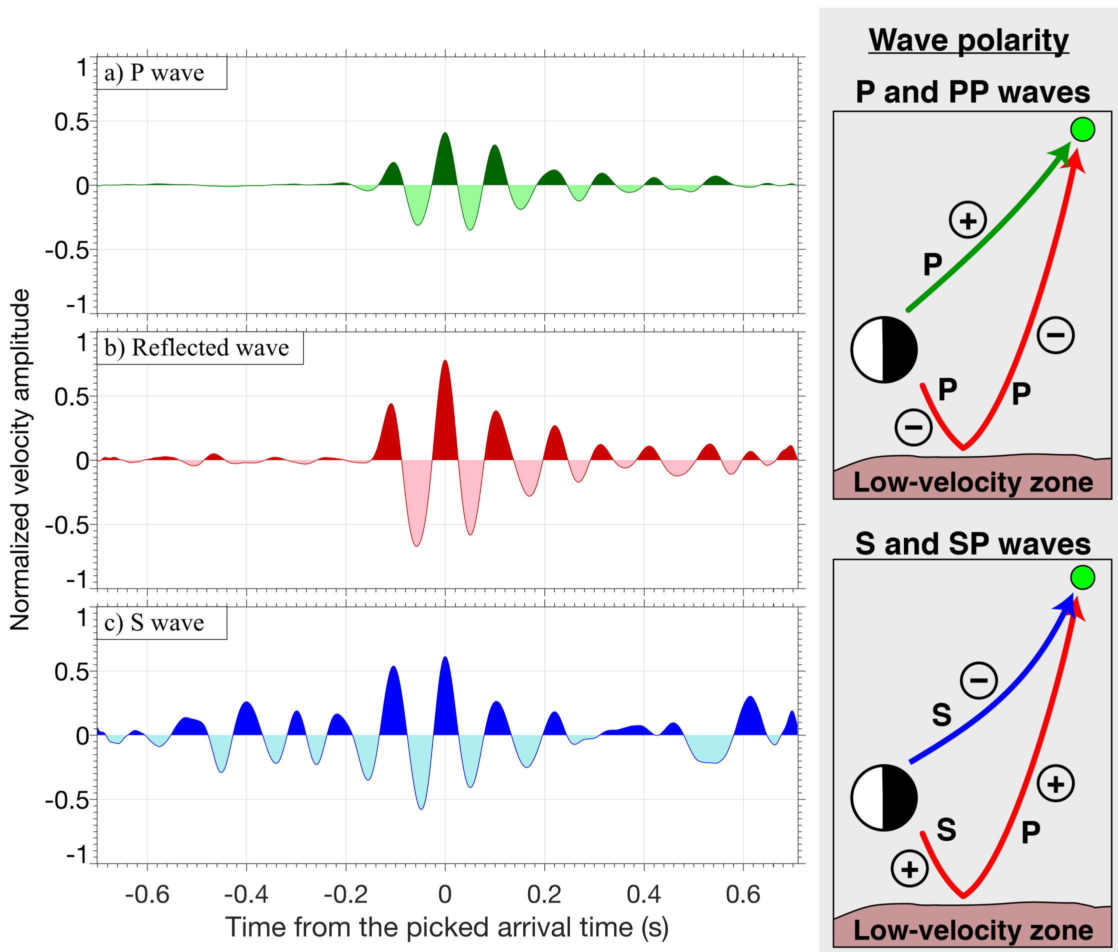

Figure 3. (a–c) Polarity of the P, reflected, and S waves averaged over all earthquakes according to the travel times shown in Figure S2. The reflected wave has the same polarity as the P wave. The positive and negative amplitudes are filled by dark and light color, respectively. The relative amplitudes between panels are preserved. The right cartoons show the theoretical polarities of P, reflected, and S waves with a projection on the vertical component; P and PP waves have opposite polarity, and P and SP waves have the same polarity.

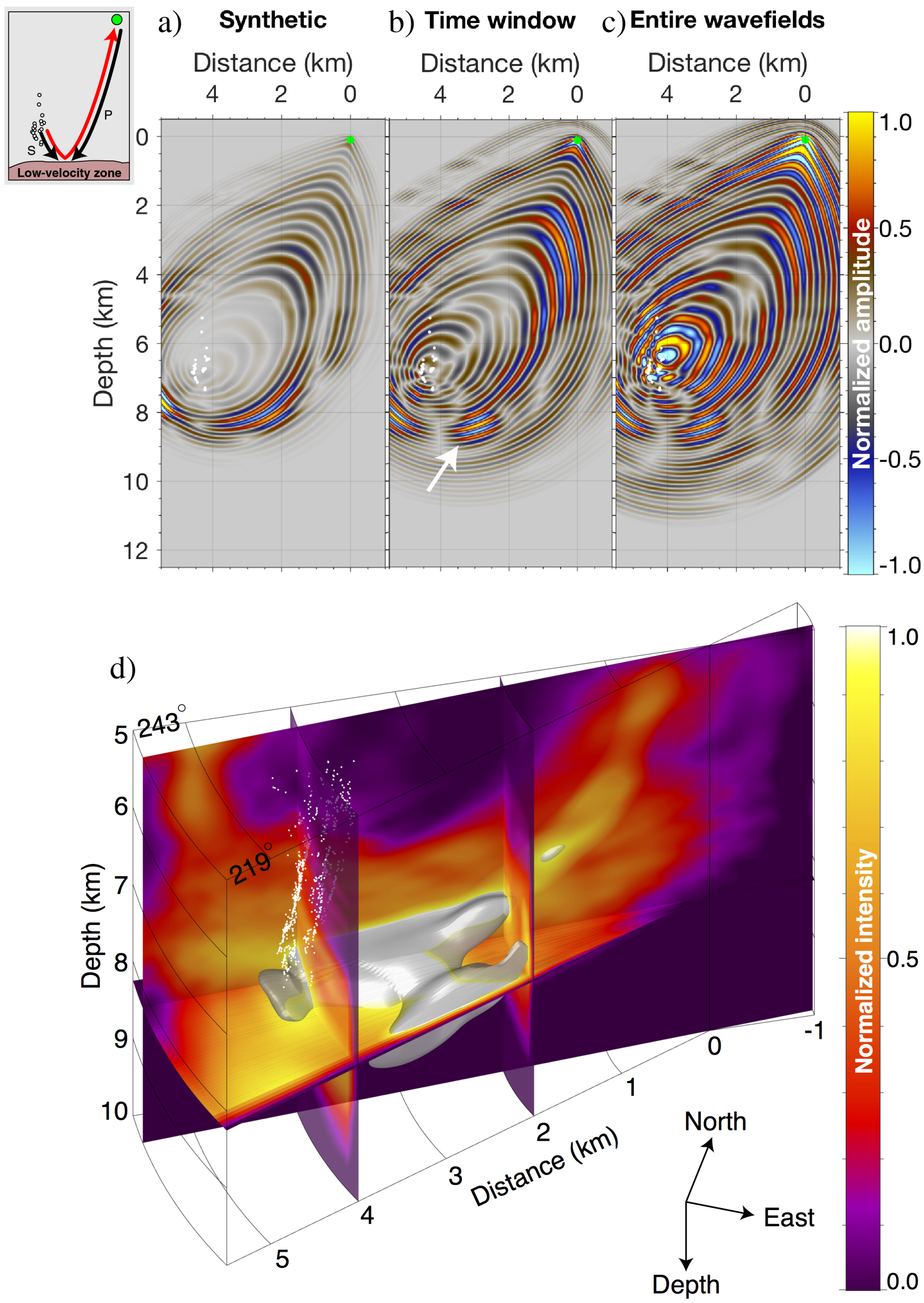

a)
Synthetic
b)
Time window
c)
Entire wavefields
Distance (km)
Depth (km)
Normalized amplitude
Low-velocity zone
P
S
d)
243°
219°
Depth (km)
Distance (km)
North
East
Depth
Normalized intensity

Figure 4. (a–c) Image at azimuth 225° obtained by the wavefield migration as SP reflection. The green and white dots show the location of station MLH and earthquakes on this plane, respectively. Images on the left, middle, and right columns are constructed from synthetic, time-windowed, and entire wavefields (i.e., Figure 2). The synthetic wavefields are the same as the waves used in Figure S1a. The time window used for panel (b) isolates wavefields at the picked travel time of the reflected wave ± 1 s. The white arrow in panel (b) highlights the target image portion for the target reflector. The amplitudes of the images are individually normalized in each panel. The top-left inset shows a cartoon for the imaging procedure, where the red arrow indicates the observed data and the black the numerically extrapolated wavefields for imaging. (d) Intensity of the migrated images in the 3-D view with the assumption of SP reflection after combining all 2D images in different azimuths. The area of this image is shown in Figure 1c. To compensate the number of earthquakes used for each 2D image, we normalize the intensity of each 2D image. The receiver is located at distance and depth of 0 km. The white dots show the locations of the earthquakes. The silver surface indicates the high intensity areas (isosurface: normalized intensity of 0.7), which represent inferred reflector locations.

Supporting Materials for "Imaging a crustal low-velocity layer using reflected seismic waves from the 2014 earthquake swarm at Long Valley Caldera, California: the magmatic system roof?"

Nori Nakata[1] and David R. Shelly[2]

Appendix A: 3D beamforming

When we consider the earthquake swarm shown in Figure 1 as a source array, we can apply array signal-processing techniques on the source side [*Spudich and Bostwick*, 1987]. We compute the 3D beamforming assuming that waves from the swarm earthquakes propagate as plane waves in the time domain. To understand the impulse response of this source array, we synthesize P, reflected, and S waves according to their travel times. We pick the travel times of each phase at each event (Figure S2) and make synthetic waves using a band-limited delta function at 6–12 Hz. Then we apply the 3D beamforming to

[1]University of Oklahoma, Norman, Oklahoma, USA

[2]U.S. Geological Survey, Menlo Park, California, USA

the synthetic waves (Figure S1a). The beamforming is based on slant-stacking (or $\tau - p$ transform) in the time domain [*Nakata et al.*, 2016], and we scan over 3D slownesses as a grid search to identify waves shown in the data. P, reflected, and S waves are focused at appropriate locations, respectively (highlighted by arrows), but each beam is smeared in the East-West direction because the source distribution is sparse in this direction (see Figure 1bc). Due to this sparseness, we find artifacts in the negative East slowness (also known as aliasing or cycle skipping). This also indicates that the depth and north slownesses are more reliable than the East slowness. Note that, although the assumption of the plane wave is not well satisfied here, we can interpret the beams in Figure S1 and estimate slownesses of each beam without introducing the added complexity associated with spherical wave-fronts. The violation of the assumption causes smearing of beams. If we use sub-clusters of these events as source arrays, plane-wave assumption is better satisfied because the array size becomes smaller, but signal-to-noise ratio (SNR) would be decreased due to the smaller number of sources averaging in each cluster.

Next, we beamform the observed wavefields from 0.5–4.5 s in Figure 2b (Figure S1b). Because the wavefields contain not only the three waves we are interested in, the beams are complex and more difficult to interpret than the impulse response. By using Figure S1a as a reference, we can find the beams of P, reflected and S waves in Figure S1b as well (highlighted by the arrows). Estimated slownesses for P, reflected, and S waves are (North, East, Depth) = (0.06, 0.38, -0.26), (0.10, 0.41, 0.14), and (0.10, 0.40, -0.40) in s/km, respectively. If the data satisfy the plane-wave assumption reasonably well with sufficient spatial sampling, the slowness obtained by this 3D beamforming provides a good estimate of the true wave velocity at the earthquake source region. The absolute velocities obtained by each beam location are 2.2, 2.2, and 1.7 km/s for P, reflected, and S waves, respectively; they are all too low (and similar to synthetic beams in Figure S1a) compared to the expected seismic velocities at this depth (Table S1). One possible reason of the high slownesses (low velocities) is that the discrepancy between plane and spherical wave-fronts for different sources approaches is not ignorable in this scale [*Johnson and Dudgeon*, 1993].

Because the depth slowness of the reflected wave has the opposite sign than other two waves, the reflected waves first propagate downward, reflect at an interface, and then reach the receiver at the ground surface as expected from the shape of the moveout in Figure 2b. This also indicates that the reflector is located deeper than the source region.

Appendix B: Amplitude ratios between P, S, PP, and SP waves

In this appendix, we calculate approximate amplitude ratios between direct P, direct S, reflected PP, and reflected SP waves based on our knowledge of the radiation pattern of earthquakes and structural parameters (Table S2). The event parameters are estimated from the template earthquake. Since we are interested in the ratio of amplitudes, we normalize the analytical far-field displacement amplitudes for P and S waves and ignore the time shift (adopted after Eqs. 9.22 and 9.26 in *Shearer* [2009]), which are given as

$$\begin{aligned} u^p &= \frac{\sin 2\theta \cos\phi}{rV_p^3} e_z^p \\ u^s &= \frac{-\cos\theta \sin\phi}{rV_s^3} e_z^s, \end{aligned} \tag{B1}$$

where θ is the takeoff angle from the dip, ϕ is the azimuth from the strike (see Fig. 9.7 in *Shearer* [2009] for the convention), r is the distance from the hypocenter to the receiver, V_p and V_s are the P and S velocities, respectively, and e_z^p and e_z^s are the vertical component of unit vectors related to the incident angle and the component for observation (vertical) for P and S waves, respectively. We focus on the SV component for u^s because we have only data in the vertical component. The takeoff angles for P and S waves are identical, because we assume that $\mathrm{V}_p/\mathrm{V}_s$ is constant. In our data, $\theta = 180 - 65 - 38.6 = 76.4°$ and $\phi = 48.7 - (100 - 90) = 38.7°$ for direct waves.

We assume that the distance is based on the straight path ($r = 7.2$ km for direct waves). This is accurate enough for our study by comparing the estimated takeoff angle (38.6°) [*Shelly et al.*, 2016] and the angle based on this straight-path assumption (34°). For reflected waves, based on the depth of the reflector images (Figures 4 and S4), $r = 10.8$ km and $r = 12.6$ km for SP and PP reflections, respectively. Again with the straight-path assumption, the takeoff angles for SP and PP waves are 22° and 18°, respectively.

Due to the velocity structure, the incident angle of the direct waves to the surface is 21.6°. Therefore, direct-wave amplitudes for direct P and S waves are $0.21/rV_p^3$ and $0.28/rV_s^3$, and the ratio of them (u_s/u_p) is 7.7. This ratio is much larger than our observation (Figure 3), probably because we ignore the near-surface effect, in which the low velocity at the near surface makes the propagation of the incoming waves nearly vertical. According to the amplitude ratio in Figure 3, an appropriate incident angle would be 5° and the ratio becomes 1.7. We use this incident angle for the calculation for the reflected waves.

For the analytical amplitudes for SP and PP waves, we modify Equation B1 and multiply reflection coefficients. We speculate that the low-velocity body beneath the reflecting horizon consists of partial-melt rhyolite, with an elevated V_p/V_s ratio [*Watanabe*, 1993]. With the incident angle based on the straight path, the reflection coefficient at the top of the low-velocity zone is 0.047 and -0.020 for SP and PP waves, respectively. Therefore, the amplitude ratios between these waves and the direct P wave are 0.50 (SP) and -0.024 (PP).

Although we approximate some parameters such as the incident angle and velocities below the reflector, the SP wave is significantly larger than the PP wave. The amplitude of the SP wave is comparable to direct P or S waves but not larger. This suggests that the velocity below the reflector is possibly even lower than the values on Table S2.

References

Johnson, D. H., and D. E. Dudgeon, *Array signal processing: concepts and techniques*, Prentice Hall, 1993.

Nakata, N., P. Boué, F. Brenguier, P. Roux, V. Ferrazzini, and M. Campillo, Body and surface wave reconstruction from seismic-noise correlations between arrays at Piton de la Fournaise volcano, *Geophys. Res. Lett.*, *43*, 1047–1054, doi:10.1002/2015GL066997, 2016.

Prejean, S., W. Ellsworth, M. Zoback, and F. Waldhauser, Fault structure and kinematics of the Long Valley Caldera region, California, revealed by high-accuracy earthquake hypocenters and focal mechanism stress inversions, *J. Geophys. Res.*, *107*(B12), 2355, doi:10.1029/2001JB001168, 2002.

Shearer, P., *Introduction ot seismology*, 2 ed., Cambridge, 2009.

Shelly, D. R., J. L. Hardebeck, W. L. Ellsworth, and D. P. Hill, A new strategy for earthquake focal mechanisms using waveform-correlation-derived relative polarities and cluster analysis: Application to the 2014 Long Valley Caldera earthquake swarm, *J. Geophys. Res.*, *121*, 8622–8641, 2016.

Spudich, P., and T. Bostwick, Studies of the seismic coda using an earthquake cluster as a deeply buried seismograph array, *J. Geophys. Res.*, *92*(B10), 10,526–10,546, 1987.

Stroujkova, A. F., and P. E. Malin, A magma mass beneath Casa Diablo? Further evidence from reflected seismic waves, *Bull. Seismol. Soc. Am.*, *90*(2), 500–511, 2000.

Watanabe, T., Effects of water and melt on seismic velocities and their application to characterization of seismic reflectors, *Geophys. Res. Lett.*, *20*(24), 2933–2936, 1993.

Wyering, L. D., M. C. Villeneuve, I. C. Wallis, P. A. Siratovich, B. M. Kennedy, D. M. Gravley, and J. L. Cant, Mechanical and physical properties of hydrothermally altered rocks, Taupo Volcanic Zone, New Zealand, *J. Volcanol. Geoth. Res.*, *288*, 76–93, 2014.

List of tables

Table S1. One-dimensional velocity model.

Depth (km) to top of layer	P velocity (km/s)	S velocity (km/s)
0.0	3.55	1.98
0.5	3.57	1.99
1.0	3.70	2.07
2.0	4.55	2.54
3.0	5.05	3.12
4.0	5.67	3.20
5.0	5.75	3.30
6.0	5.90	3.41
7.0	5.99	3.44
8.0	6.00	3.48
9.0	6.04	3.49
10.0	6.06	3.50
12.0	6.07	3.51

This velocity model is based on *Stroujkova and Malin* [2000] and *Prejean et al.* [2002].

Table S2. Parameters of earthquake sources and structural velocities.

Parameter name	values
Azimuth to station MLH*	48.7°
Takeoff angle* (0°=up, 180°=down)	38.6°
Strike, Dip, Rake*	(100°, 65°, 179°)
P velocity in near surface**	3.55 km/s
P velocity at hypocenter†	6.00 km/s
V_p/V_s†	1.79
P velocity below the reflector‡	5.40 km/s
S velocity below the reflector‡	2.70 km/s

* *Shelly et al.* [2016]; ** *Prejean et al.* [2002]; † *Stroujkova and Malin* [2000]; ‡ *Watanabe* [1993] and *Wyering et al.* [2014]

List of figures

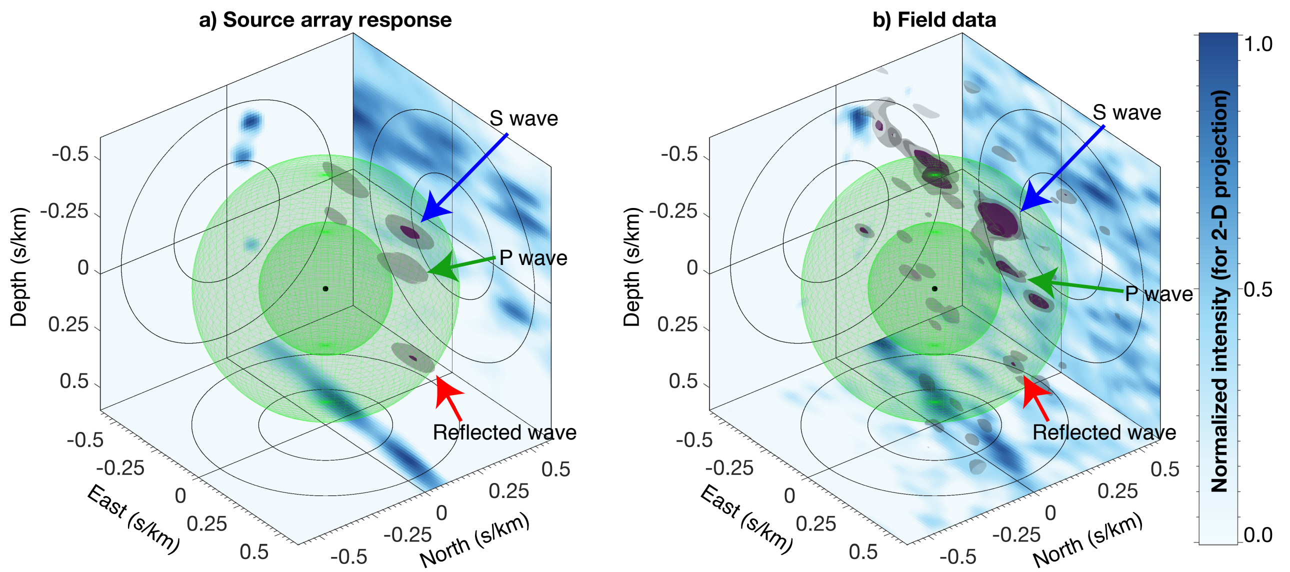

Figure S1. Intensity of 3D beamforming at the array of earthquake swarm sources in the slowness domain. The gray and purple surfaces show the isosurfaces of the intensity at two different levels. The green balls indicate slownesses of 0.25 and 0.5 s/km, and the black dot is the origin of the beam domain. Each plane shows the 2D projection of the intensity (average over the normal direction to the plane). (a) 3D beams obtained from synthetic band-limited delta functions, which contains P, reflection, and S waves based on the picked travel times in Figure 2. This beam illustrates the source array response for the spatial distribution of the events used. (b) 3D beams obtained from the wavefields shown in Figure 2a at 0.5–4.5 s. The arrows highlight the beams for P, reflection, and S waves.

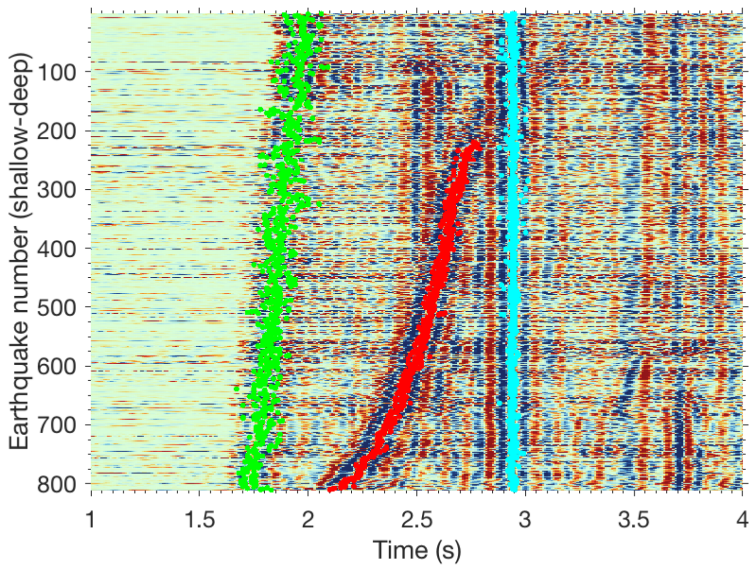

Figure S2. Picked travel times shown on the waveforms in Figure 2b. The green, red, and cyan dots correspond to P, reflection, and S wave arrival times (with positive amplitudes), respectively. We pick the arrival time of reflected waves at only earthquakes 221–811 because reflected waves of shallower events are weaker and simultaneously arrived with other phases.

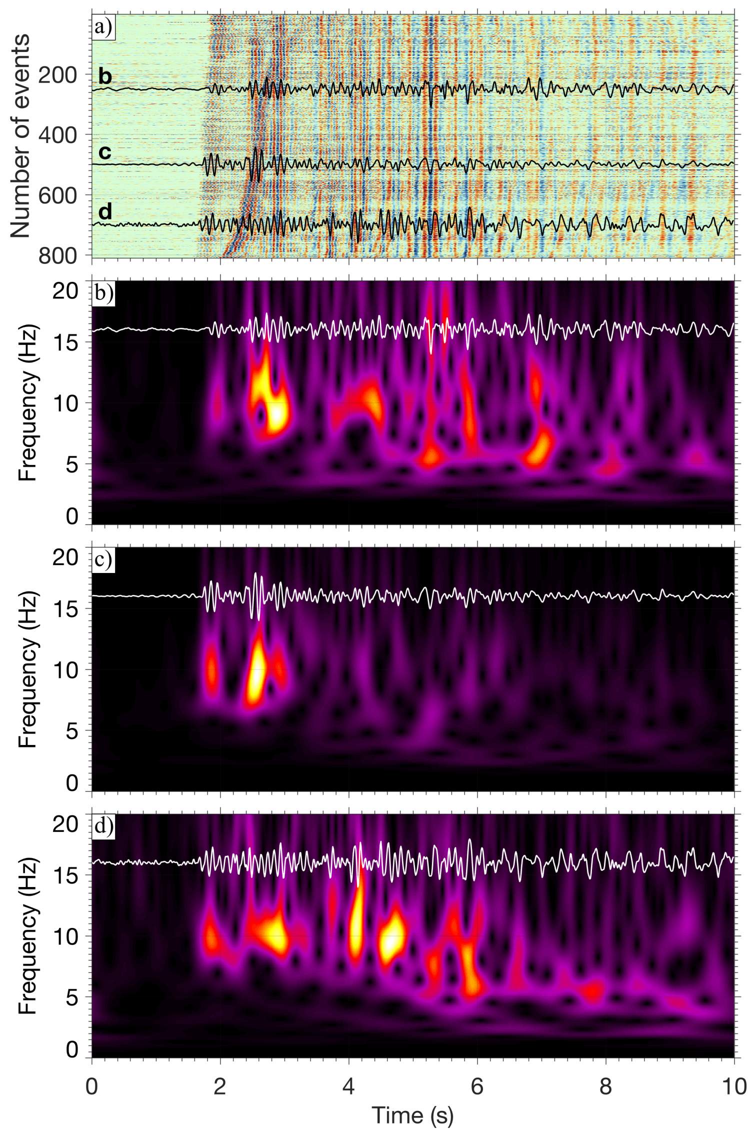

Figure S3. (a) Observed event waveforms (same as Figure 2b), and time-frequency spectrogram for events (b) 250, (c) 500, and (d) 700. The black lines in panel (a) highlight the waveforms used in panels (b–d) and are the same as the white lines in each panel.

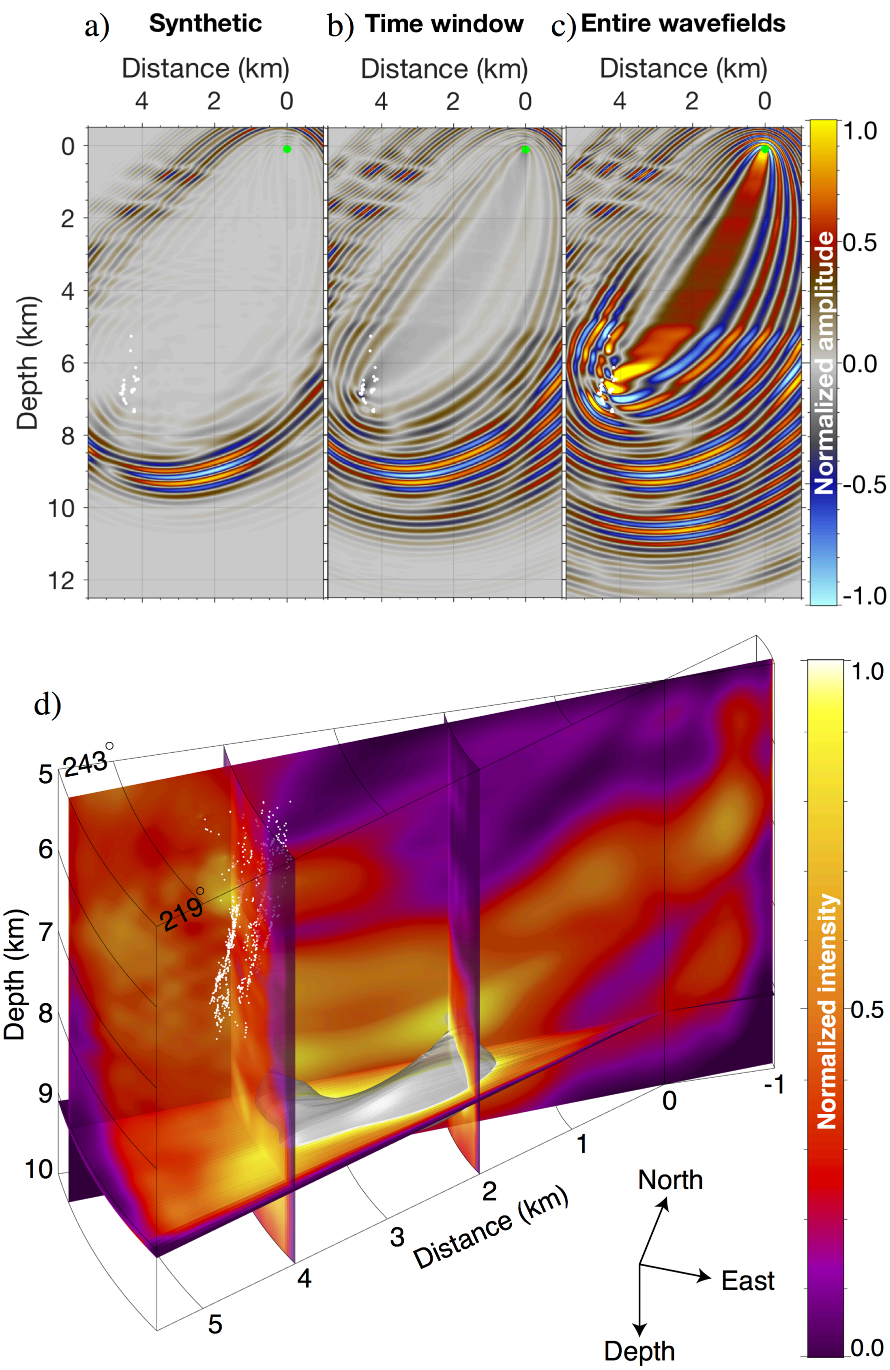

Figure S4. Same as Figure 4, but for the assumption of PP reflections.